AIAA JOURNAL
Vol. 45, No. 7, July 2007

Visualization and Measurement of Flow over a Cylindrical Surface with a Bump

Murat Tutkun,* Peter B. V. Johansson,† and B. Anders Pettersson Reif‡
Chalmers University of Technology, 412 96 Gothenburg, Sweden

DOI: 10.2514/1.27982

The complex flowfield around a cylindrical bump with a hemispherical free end mounted on a cylindrical surface has been studied by means of liquid-crystal flow visualization, surface-pressure measurements, and cross-hot-wire anemometry. This setup constitutes a prototype of a typical wall-mounted sensor on an aircraft. The slenderness parameter of the bump is one and the curvature of the hemispherical ending starts at the half-height of the bump. The radii of both the cylindrical and hemispherical parts of the bump are equal. The thickness of the turbulent boundary layer over the cylindrical surface, which controls the location of the separation over the bump's surface, is smaller than the bump height at the position at which the bump is located. The flow over the hemispherical free end separates further downstream than does the flow over the cylindrical part of the bump. The size of the recirculation region downstream of the bump is larger than the recirculating region of a finite cylinder with a flat end. A Reynolds number dependence of the reattachment point behind the bump is observed. Large turbulence fluctuations exist because of the interaction between the downwash and the turbulent boundary layer developing over the ground surface. The upstream disturbance of the bump, retardation due to an adverse pressure gradient, and push up of the flow due to the finite length of the bump are also captured by the velocity measurements. Effects due to the curvature of the surface plane are not detectable far downstream of the bump.

Nomenclature

C_p	=	pressure coefficient
C_{pb}	=	base pressure coefficient
D	=	diameter of the bump, m
H	=	height of the bump, m
H/D	=	slenderness parameter
p	=	static pressure, Pa
p_{atm}	=	atmospheric pressure, Pa
p_{dyn}	=	dynamic pressure, Pa
Re	=	Reynolds number based on the bump diameter, DU_∞/ν
S	=	coordinate direction on the circular plate's periphery
s	=	coordinate direction along the bump's surface
U_i	=	mean velocity in the x_ith direction $[U_1, U_2, U_3] = [U, V, W]$, m/s
U_∞	=	freestream velocity, m/s
u_i	=	root mean square of fluctuating velocity in the x_ith direction $[u_1, u_2, u_3] = [u, v, w]$, m/s
$\langle u_i u_j \rangle$	=	Reynolds stress, m^2/s^2
x_i	=	Cartesian coordinates $[x_1, x_2, x_3] = [x, y, z]$
Δp	=	relative pressure ($p - p_{\text{atm}}$), Pa
δ	=	boundary-layer thickness, m
ν	=	kinematic viscosity, m^2/s
ρ	=	fluid density, kg/m^3

Presented as Paper 3140 at the 25th AIAA Aerodynamic Measurement Technology and Ground Testing Conference, San Francisco, CA, 5–8 June 2006; received 23 September 2006; revision received 12 February 2007; accepted for publication 11 March 2007.

*Ph.D. Student, Department of Applied Mechanics; murat.tutkun@chalmers.se.

†Assistant Professor, Department of Applied Mechanics; peter.johansson@chalmers.se. Member AIAA.

‡Adjunct Professor, Department of Applied Mechanics; also Principal Scientist, Norwegian Defence Research Establishment (FFI), P.O. Box 25, NO-2027, Kjeller, Norway; Bjorn.Reif@ffi.no. Member AIAA.

I. Introduction

FLOWS around bluff-cylinder-like structures are commonly encountered in a large variety of fluid dynamics applications related to safety issues such as bridges, offshore installations, and aviation safety. The flow-induced forces exerted by these bluff bodies are usually time-varying and therefore of concern in, for example, the design of structures susceptible to fatigue. The prototype problem of wall-mounted circular cylinders has been studied extensively over the years (e.g., Chen [1]) because of its simple geometry and features of the bluff-body wake structures. In most applications, the two-dimensional approximation does not apply, because of the limited span of the cylinders.

Wall-mounted bluff bodies that extend across external boundary layers into the freestream are present in many aero- and hydrodynamic applications such as radomes mounted on aircraft or underwater vehicles. Although the size of these devices is usually small compared with the overall size of the vehicle, they can have a severe impact on the performance and in some cases can even impose highly undesirable operational restrictions.

Boundary layers developing along surfaces with transverse curvature are also often encountered in practice. The vast majority of studies were concerned with plane surfaces. In most situations, however, the boundary-layer thickness is significantly smaller than the radius of transverse curvature, and so curvature effects can be neglected. The situation can be considerably altered by mounting an obstacle with sufficient height on the surface. The recovery of the massively separated flow region downstream of the bluff body might then be affected by the transverse curvature, and the plane surface approximation becomes no longer valid.

The endwall effects are very different in the case of finite length bluff bodies. The presence of the ground surface will force the flow toward a two-dimensional state, because the wall-normal velocity component is suppressed in the vicinity of the wall [2]. The flow immediately downstream of the obstacle is characterized by an intricate interaction between the incoming boundary layer and the horseshoe vortices generated immediately upstream of the obstacle. The free end of the body will also contribute to a significant three-dimensionalization of the flowfield and will continuously generate arch, or wake, vortices that shed downstream [3]. Experimental results by Szepessy and Bearman [2] and Sakamoto and Arie [3] suggested that these wake vortices dominate the unsteady forcing of small-aspect-ratio cylinders. The importance of the wake vortices

was further elucidated by Farivar [4], who found that the level of fluctuating pressure peaked very close to the free end, rather than in the region in which the classical infinite cylinder applies. Ayoub and Karamcheti [5] investigated the flow in the tip region of a circular cylinder with a slenderness parameter (or height-to-diameter ratio) of $H/D = 12$ and were able to show that the shedding frequency of this region is different from the rest of the cylinder. Studies on the effects of the slenderness parameter have revealed the complexity of the wake structures behind finite size bodies. When the slenderness parameter is smaller than a critical value, the von Kármán vortex (which is the dominant flow structure in the case of infinite and/or large-aspect-ratio cylinders) is suppressed, and the interaction of trailing vortices from the free end, horseshoe vortices from the sides of the cylinder, and separation create a highly unstable and complex turbulent wake behind the finite length bluff body (see Okamoto and Tagita [6], Etzold and Fiedler [7], Kawamura et al. [8], Sumner et al. [9], and Pattenden et al. [10]).

The flow structure behind the finite length cylinder is also highly dependent on the shape of the free end of the bluff body. Leder [11] studied possible influences of a hemispherical end shape by examining the vortex structures, the size of the recirculating region, and the turbulent kinetic energy for $H/D = 2$. He showed that the strength of the counter-rotating trailing vortices for a hemispherical end was significantly smaller than for a flat end on which sharp edges are present. The counter-rotating trailing vortices created a downward motion along the plane of symmetry and affected the size of the recirculating region. Therefore, the recirculating region was larger for the case of a finite cylinder with a hemispherical end. A similar investigation was carried out by Park and Lee [12] for finite cylinders of $H/D = 6$ with different free ends: flat, beveled, radiused, and hemispherical. Similarly, they reported that the trailing vortices created at the tip of the cylinder got weaker and almost disappeared when the sharp corner of the free end was rounded into a smooth shape. They also observed that the end effect suppressed the von Kármán vortex, regardless of the shape of the free end.

Recently, numerical simulations of the flow around finite cylinders were performed by Fröhlich and Rodi [13] and Pattenden et al. [14] using large eddy simulation and detached eddy simulation. These simulations also showed the complexity and three-dimensionality of the flow behind the finite height cylinders and the suppression of the von Kármán vortex due to downwash from the free end.

The wall-mounted obstacle also has an upstream effect, because an adverse pressure gradient is created that deflects the incoming two-dimensional boundary layer so that it becomes strongly three-dimensional [15]. The three-dimensionality is mainly characterized by the continuous generation of one or more horseshoe-shaped vortices that wrap around the base of the obstacle [10]. These vortices interact strongly with the near-wake downstream of the obstacle, and the interaction increases with increased ratio between boundary-layer thickness and obstacle height.

In the present study, a cylindrical bump with a hemispherical free end is mounted on a cylindrical surface to model a wall-mounted sensor (radome) on the aircraft Orion P-3C [16]. The motivation for the study is to gain physical insight into the generation mechanisms for flow-induced vibration observed on the aircraft. The ultimate goal is to devise countermeasures for control, but this is outside the scope of the present study. The primary objectives of the present study are to 1) provide experimental data to be used for verification and development of computational fluid dynamics models and 2) investigate the effects of different Reynolds numbers. The reported data consist of two-component instantaneous velocity measurements using a cross-hot-wire probe, static surface-pressure measurements, and surface-flow-pattern visualizations using shear-stress-sensitive paint.

II. Experimental Setup

The experiments were performed in the L2 wind tunnel of Chalmers University of Technology. This is a low-turbulence wind tunnel with a freestream streamwise turbulence intensity less than 0.03%. The cross-sectional area and the length of the test section are 1.80×1.25 m^2 and 3.00 m, respectively. The maximum speed of the tunnel is 60 m/s. The temperature uniformity of the tunnel is maintained to within an accuracy of ± 0.05°C. A pitot tube, an absolute pressure sensor, and a temperature sensor were connected to a Furness FCO510 micromanometer to monitor the wind-tunnel velocity. The tunnel velocity was sent to the computer directly via the RS232 port.

The model placed into the wind tunnel consisted of a cylindrical surface and a bump mounted on top of the cylinder (see Fig. 1). Both the height and the diameter of the bump were 100 mm, corresponding to a slenderness parameter of 1. The free end of the bump was hemispherical and the curvature of the ending starts at the half-height of the bump. The radius of the hemispherical part was 50 mm. The bump was placed 1000 mm downstream of the leading edge of the circular ground plate. Special attention was given to the leading edge of the plate to prevent flow separation. The incoming fully turbulent boundary layer was thinner than the bump height at the position of the bump ($\delta/D = 0.15$).

The friction-line pattern over the cylindrical surface was visualized using shear-stress-sensitive paint (Hallcrest, Inc. BCN-192). The paint was composed of liquid crystals, and the principle of operation of the paint was that when it was subjected to a shear force, the color of the paint changed as the shear stress magnitude and the direction of the shear vector changed [17]. Flow visualization using this paint provided the footprint of the flow over the surface. The area covered by the paint extended 30 mm upstream of the bump, 100 mm in the spanwise direction from the centerline, and 500 mm downstream of the bump.

Static pressures on both the cylindrical surface and the bump were measured using flush-mounted pressure taps. The holes on the cylindrical surface are visible in Fig. 2a. The pressure taps were connected to a Scani-valve pressure recording system that was capable of scanning 50 channels in a sequence to the Furness FCO510 manometer. The recording time at each channel was set to 1 min to get statistically accurate readings, and the resulting time-averaged pressure was written to the computer's disk. The accuracy of the pressure transducer was better than $\pm 0.25\%$, but the overall accuracy depended on how well the pressure taps were fabricated. In this case, stainless steel tubes with an inner diameter of 1.6 mm and an outer diameter of 1.8 mm were cut in 1-cm-long pieces. Holes with the same diameter as the inner diameter of the tubes were drilled through the bump and the circular surface. Then holes having the same diameter as the outer diameter of the tubes were drilled halfway through from the inside, after which the tubes were mounted using glue. Finally, the surface was sanded to ensure a smooth surface. Thin silicon tubes were used to connect the pressure taps to the manometer. The relative pressure ($\Delta p = p - p_{\text{atm}}$) on the plate was measured at two different Reynolds numbers: 33,000 and 200,000.

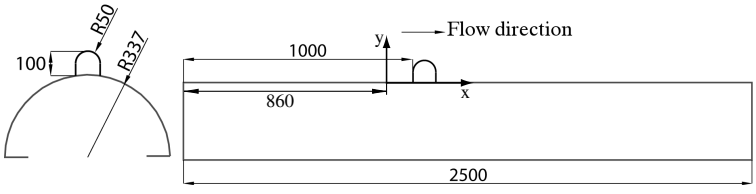

a) Front view **b) Side view**

Fig. 1 Schematic of the model; all dimensions are in millimeters.

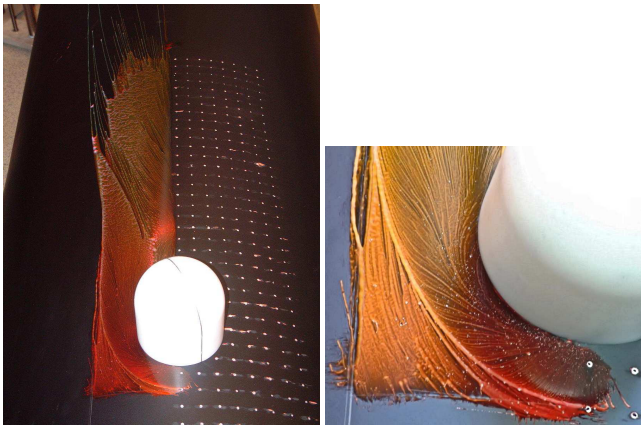

a) Front view

b) Close-up of the area immediately upstream of the bump

Fig. 2 Flow visualization using liquid-crystal coating.

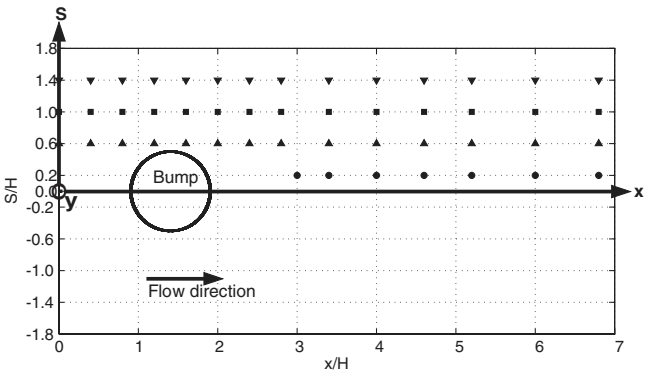

Fig. 3 Top view of the setup and the measurement grid of the cross-wire probe with the coordinate system: the S axis is tangent to the surface of the circular ground surface; all X–Y planes are to the X–Y plane on the symmetry line of the circular ground surface at $S = 0.0$; and the leading edge of the ground surface is at $x/H = -8.6$.

Measurements at two additional Reynolds numbers (67,000 and 133,000) were performed to obtain the pressure distribution over the bump. The pressure taps over the circular plate were placed in an area of 700 mm in the streamwise direction times 160 mm radially out from the centerline symmetry plane. The distance between the pressure taps was 20 mm in both directions. The total number of the pressure taps was 261 on the cylindrical surface and 63 on the bump's surface. The maximum uncertainty in the pressure measurements was less than 1% in total.

Velocity measurements were performed using a cross-hot-wire probe. The probe was manufactured at the Turbulence Research Laboratory of Chalmers University of Technology, and the details of the probes were documented by Johansson and George [18]. The sensing wire (Dantec) was made of tungsten, with a diameter of 5 μm and a length of 3 mm. The probe was connected to a two-channel DISA 56C17 constant temperature anemometer (CTA) system, and the data were digitized using an IO Tech Wavebook 516 16-bit, 1-MHz sample-and-hold A/D converter. The data were sampled at 250 Hz, and 10,000 samples were taken for each CTA channel at each measurement location. One of the main concerns about cross-wire measurements is the response of the probes in high-turbulence intensity and separated flows, because the sensors of the probe are insensitive to the direction of the flow. When the cross wire is placed into highly three-dimensional flow, it leads to large errors in the results, especially for the second-order moments (e.g., approximately 30% error when the turbulence intensity is 35%) [19]. Therefore, the measurement grid was designed not to have the probe inside a high-turbulence-intensity flow or a separated and recirculating region. The first plane of measurements started 20 mm away from the centerline of the cylinder and 110 mm behind the bump, to avoid the recirculating zone in the vicinity of the bump. Three more planes (60, 100, and 140 mm away from the centerline of the cylinder) were also measured. For these three planes, the investigated area extended upstream of the bump by 90 mm. All of the measurements were made between 5 and 200 mm along the y axis. It should be noted that a Cartesian coordinate system was used for the measurement. The measurement grid in the streamwise–spanwise (X–Z) plane can be seen in Fig. 3.

A round jet with very-low-turbulence intensity was used for calibration of the cross-hot-wire probe. The probe was calibrated between ± 30 deg with 10-deg increments. For each angle, different jet velocities were adjusted between 4 and 16 m/s. Following Champagne et al. [20], effective cooling velocities for the cross-wire arrangement were written in terms of magnitude of the flow velocity, the angle between the normals to the wires and the mean flow direction, and yaw coefficients. The effective cooling velocities were expanded using the linearization scheme detailed in George et al. [21]. The resulting nonlinear equations were solved using a nonlinear least-squares method described by Glauser [22]. Using this method, an accuracy of $\pm 0.5\%$ was determined. The relative uncertainty of 3.5% for the 95% confidence interval, including uncertainties due to the calibration, was achieved for each velocity sample that was converted from the hot-wire-anemometry output; 10,000 velocity samples for each measurement position provided 0.5% uncertainty in the mean velocity measurements for the 95% confidence level. The uncertainty of the root mean square of fluctuating velocities was 1.4% and that of the Reynolds shear stress was 3%.

III. Results

A. Flow Visualization

Liquid-crystal coating (LCC) has been used by aerodynamicists to measure the magnitude and the direction of surface shear stress based on the physical characteristics of the coating, or paint, which changes its color when it is subjected to a shear force [17,23]. In practice, this change of color is difficult to interpret for quantitative measures of the shear stress, but the paint was nevertheless found to be very useful to visualize the footprint of the mean shear stress on the surface, regardless of the color differences. Figures 2 and 4 present the patterns seen from the flow-visualization experiment. Figure 2a, shows the patterns observed from the front. It demonstrates some features of the horseshoe vortex and also the extent of the wake width downstream of the bump, where the bump is the white part. The surface-pressure taps can be seen on the right-hand side of the centerline. Figure 2b zooms into the front part of the bump, on which the friction lines and the average thickness of the horseshoe vortex can be easily seen. Recent particle image velocimetry measurements by Pattenden et al. [10] showed the unsteadiness in the horseshoe-vortex system, which consists of a continuous formation, translation, decay, and merge of the vortices upstream of the body. Hence, the sizes of the horseshoe vortices change instantaneously in time, due to the unsteady nature of the phenomenon; therefore, Fig. 2b corresponds to the time-averaged footprint of the horseshoe-vortex system. Some quantitative results can also be extracted from the photograph, because the holes for the pressure taps create a means of scale (the distance between the pressure taps are 20 mm in every direction). The average thickness of the horseshoe vortex upstream of the bump can therefore be estimated to be 30 mm, which corresponds to about 30% of the bump height.

The width of the wake covering the whole painted area (which is about 100 mm from the centerline) can be measured using Fig. 2a. The wake width is approximately constant until 100 mm (i.e., one bump height) downstream of the bump, from which the wake grows out from the originally painted area. Figure 4 also shows a side view of the imprint of the flow structures on the cylindrical surface. It should be noted that the change in the paint color from the right-hand side to the left-hand side in this figure is attributed to the angle at which the camera was held as this particular photograph was taken and does not indicate varying shear stress.

B. Surface-Pressure Measurements

Figure 5 presents the measured pressure coefficients, $C_p = \Delta p/(\frac{1}{2}\rho U_\infty^2)$, over the circular ground surface at two different Reynolds numbers: $Re = 33,000$ and $Re = 200,000$. Although there were some technical difficulties in reading the pressure from the taps located upstream of the bump for the low Reynolds number case, it is clear that the upstream C_p level of the low Reynolds number flow is significantly smaller than that of the high Reynolds number flow. Because the freestream velocity is higher for the high Reynolds number case, one can expect to see a lower static pressure level over the plate upstream of the bump. On the other hand, the flow in this region is highly affected by the adverse pressure gradient created by the presence of the bump. The upstream spanwise vorticity in the boundary layer creates a horseshoe vortex in the stagnation region of the bump. It is folded around the base of the bump and creates a pair of streamwise vortices downstream of it. Therefore, the large C_p values in the high Reynolds number case is attributed to the strength of the adverse pressure gradient and the size of the unsteady horseshoe-vortex system.

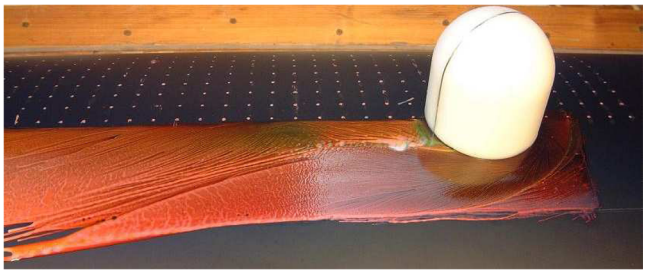

Fig. 4 Flow visualization showing the reattachment point.

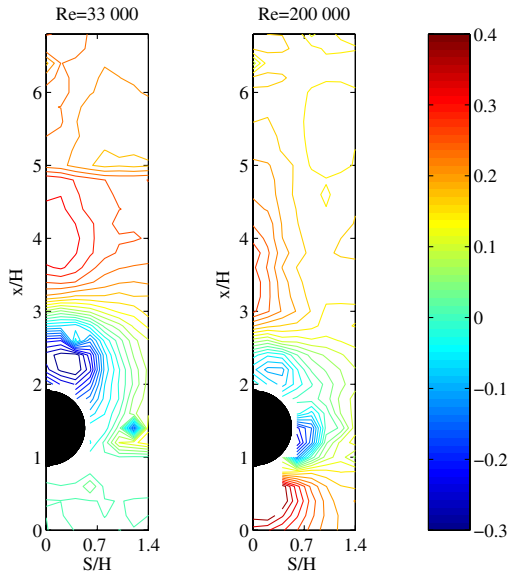

Fig. 5 C_p distribution over the circular ground surface. The increments between the contour lines is 0.04.

The pressure contours over the circular surface (Fig. 5) show the size of the recirculating region behind the bump. In this experiment, the Reynolds number is the main parameter affecting the distance between the bump and the reattachment point on the circular ground surface. Increasing the freestream velocity results in a turbulent boundary layer over the bump surface itself that delays the flow separation [24]. As clearly seen in Fig. 4, the separated flow reattaches to the circular ground approximately one diameter downstream of the bump. It should be recalled that this is a time-averaged result. Downstream of the reattachment point, there is a high-pressure region, after which the flow spreads aside and accelerates (Fig. 5, $Re = 200,000$). The surface pressure behind the bump decreases in both the streamwise and spanwise directions, meaning that there is an increase in velocity in these directions. For the low Reynolds number case (Fig. 5, $Re = 33,000$), there are no distinct features showing either acceleration or retardation of the flow in these directions. The pressure drop appears further downstream at positions around $x/H = 6$. This can be attributed to the natural pressure drop over the plate, not to acceleration of the flow in that direction.

The pressure distribution over the bump is presented in Fig. 6. (Notice that the readings for $Re = 200,000$ at 90 deg are missing in the plot, due to a technical failure during the experiment.) At the half-height of the bump, $s/H = 0.5$, the curvature of the hemispherical free end begins. On the cylindrical part of the bump, all of the curves in the plots are parallel to the vertical axis. Once the curvature of the free end is reached, differences appear on the pressure coefficients, due to the acceleration of the flow. The change in the pressure coefficients is more obvious for the 0-deg case, which is the stagnation line along the bump's height. The drop in pressure is less for the other angles and gets weaker as the flow approaches the separation. After the separation, the pressure coefficient stays approximately constant at the so-called base pressure coefficient, which is the pressure coefficient at 180 deg [25].

Below the line on which the curvature of the free end begins, the pressure distribution shows the same patterns as the pressure distribution over the finite cylinders (cf. Fig. 6 of Uematsu and Yamada [26] and Fig. 5 of Kawamura et al. [8]). For the two low Reynolds number cases in this study, the flow separates upstream of 90 deg on the cylindrical part of the bump. By contrast, for the high Reynolds number cases, the flow separates downstream of 90 deg on the cylindrical part. This is fully consistent with Achenbach [24], who studied the circular cylinder in crossflow for different Reynolds numbers by categorizing them as subcritical, critical, and supercritical Reynolds numbers. Reynolds numbers 33,000 and 67,000 in this study can be considered, based on the work by Achenbach, as subcritical Reynolds numbers. Above $s/H = 0.5$, the flow attaches to the surface, even for the low Reynolds numbers, and the separation is delayed further downstream. This can be easily seen in the distribution of static pressure at 90 deg in Fig. 6. The C_p curve of $Re = 33,000$ at 90 deg stays approximately constant for all heights, due to the separation upstream of 90 deg, but peaks very near the top, indicating that the flow is attached at this location. The curve corresponding to $Re = 67,000$ at 90 deg also stays at an approximately constant value up to $s/H = 0.5$, similar to the lowest Reynolds number case; then it starts decreasing, because the

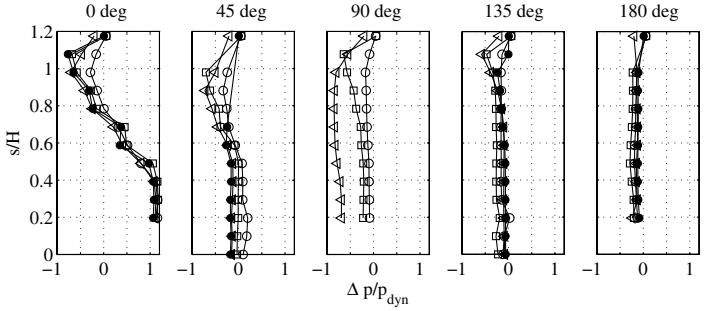

Fig. 6 C_p distribution over the bump; ○ $Re = 33,000$, □ $Re = 67,000$, △ $Re = 133,000$, and ● $Re = 200,000$.

separation is delayed further at these heights. The flow over the hemispherical part of the bump between $s/H = 0.8$ and 1.2 accelerates, and this causes the pressure coefficient to deviate from the base pressure coefficient. As seen in the plot of 90 deg, the C_p curve of $Re = 67,000$ approaches that of $Re = 133,000$. The Reynolds numbers 133,000 and 200,000 can be considered as supercritical Reynolds numbers, and the flow in this case separates around 120 deg [24]. The flow never separates on the top of the free end of the bump at the Reynolds numbers considered here. The pressure taps located closest to the top of the bump showed that for all the Reynolds numbers in this study (except $Re = 33,000$), the flow stays attached to the bump's surface, even at 135 deg. The lowest Reynolds number case, $Re = 33,000$, separates before 135 deg at this position.

C. Velocity Measurements

Profiles of the mean velocities, the root mean square of velocity fluctuations in the x and y directions, and the Reynolds shear stress distributions are reported for different downstream and spanwise locations in Figs. 7–12. The results are presented in the X–Y planes of the measurement grid, as shown in Fig. 3. The origin of the measurement coordinate system was placed on the symmetry line of the circular ground surface and 860 mm downstream of the leading edge, as presented in Fig. 1b. All X–Y planes of measurement were parallel to the X–Y plane located on the centerline of the circular ground at $S/H = 0.0$, meaning that the y axes were normal to the ground surface only on the symmetry line. The first point of measurement in the y direction was always 5 mm away from the surface ground. The Reynolds number during the cross-wire measurements was kept constant at 67,000, which corresponds to a subcritical Reynolds number. There were four different X–Y planes of measurement, as presented in Fig. 3. The first plane of measurements, $S/H = 0.2$, started at $x/H = 3.0$, which was just after the reattachment point for Reynolds number 67,000. (The reason for starting the first measurement plane at $x/H = 3.0$ was the inability of the cross wire in the highly three-dimensional recirculating flow, as explained earlier.) Other planes ($S/H = 0.6$, 1.0 and 1.4) extended further upstream, starting at $x/H = 0.0$. All of the measurement planes in the streamwise direction extended up to $x/H = 6.8$.

Figure 7 presents the normalized mean velocity vectors at different streamwise and spanwise directions. The first plane of measurements, $S/H = 0.2$, clearly shows the downwash coming from the top of the hemispherical end of the bump. The vertical motion in the negative y direction is visible until the end the of measurement grid in the streamwise direction on this plane. The highest velocity magnitude is directed toward the ground, as presented in Fig. 9, is observed at $y/H = 1$ at the first streamwise location downstream of the bump and is shown by the manner in which the peak in the V for following streamwise positions approaches the ground surface. An induced motion due to the downwash toward the ground surface exists at all measured locations in this plane.

The bump, as a bluff body, creates a turbulent wake, the velocity deficit for which is presented in Figs. 7 and 8. As seen in these figures, the velocity deficit is about 50% of the freestream velocity at $x/H = 3$ at the first spanwise plane of the measurement. The large deficit dies off quickly, due to the development of the large turbulent boundary layer ($\delta \sim 2H$ at $x/H = 6.8$) over the circular ground surface.

The root mean square of the velocity fluctuations in the x and y directions (u and v, respectively) show large fluctuations, as seen in Figs. 10 and 11. The v component in the first profile of the first spanwise plane peaks about $y/H = 1$, and this peak for the next streamwise locations moves toward the circular ground surface. The same behavior is also observed in the Reynolds shear stress distribution in Fig. 12. These peaks in the profiles can be attributed to interaction between the downwash coming from the top of the bump and the turbulent boundary layer developing over the surface after the reattachment point. Figure 8 also shows the acceleration of the flow in the near-wall region from $x/H = 3.0$ to 6.8. This is consistent with the findings of surface-pressure measurements on the circular ground surface, as shown in Fig. 5.

As mentioned earlier, the second spanwise plane, $S/H = 0.6$, started from $x/H = 0.0$ and extended to $x/H = 6.8$. It can be seen from the measurement grid (Fig. 3) that this plane was very close to

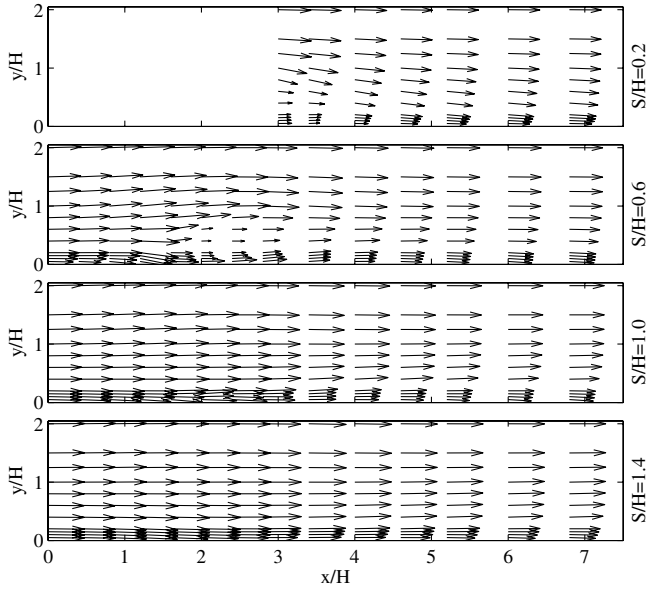

Fig. 7 Normalized mean velocity vectors for different X–Y planes of measurement.

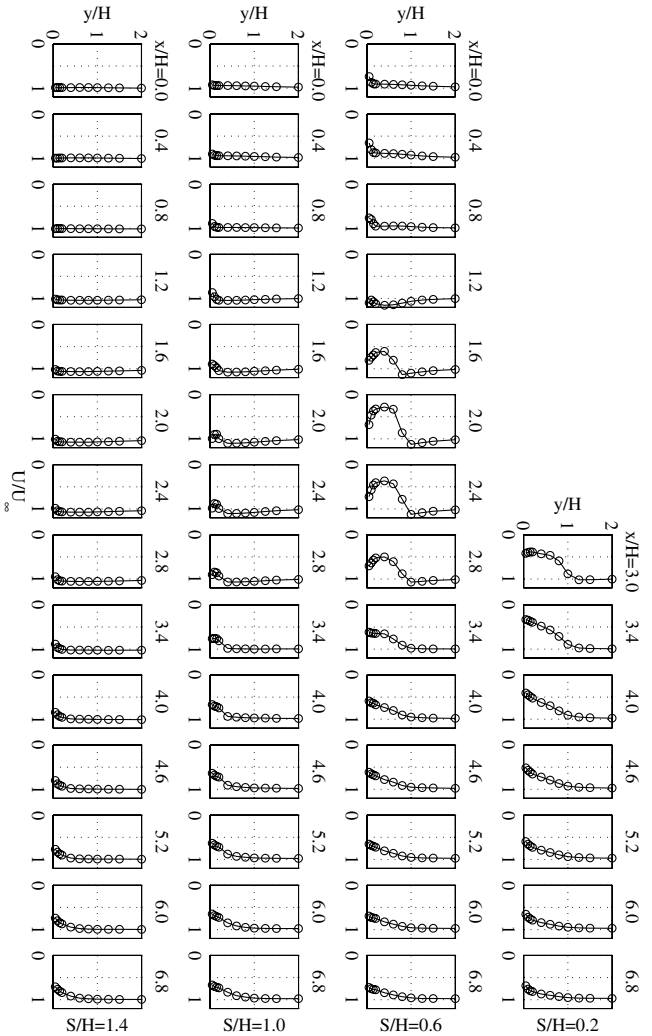

Fig. 8 Normalized profiles of mean velocities in the x direction.

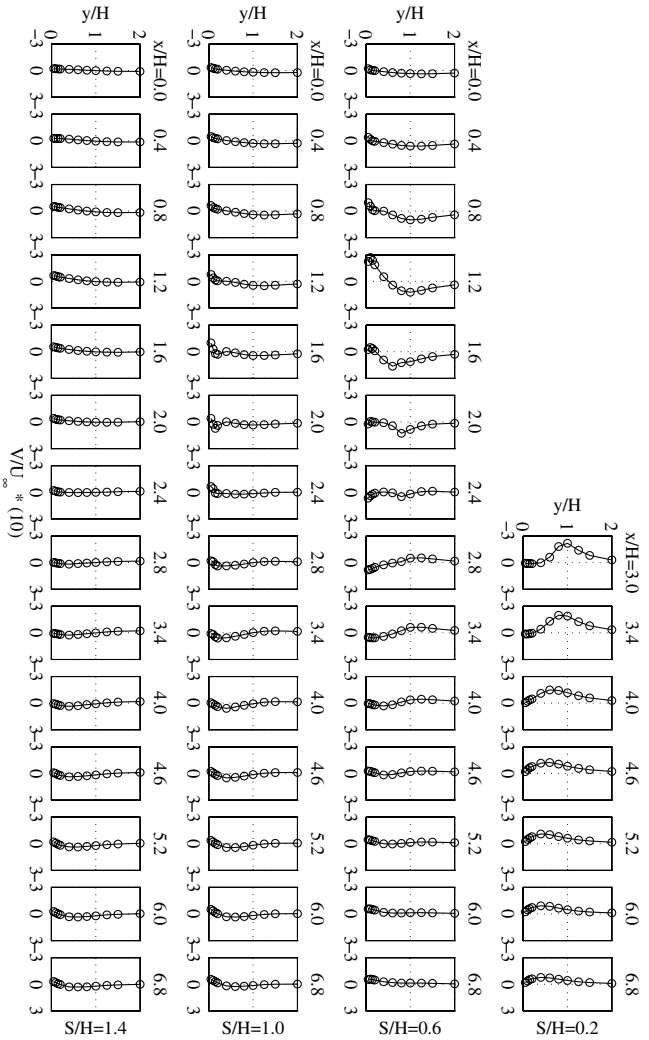

Fig. 9 Normalized profiles of mean velocities in the *y* direction.

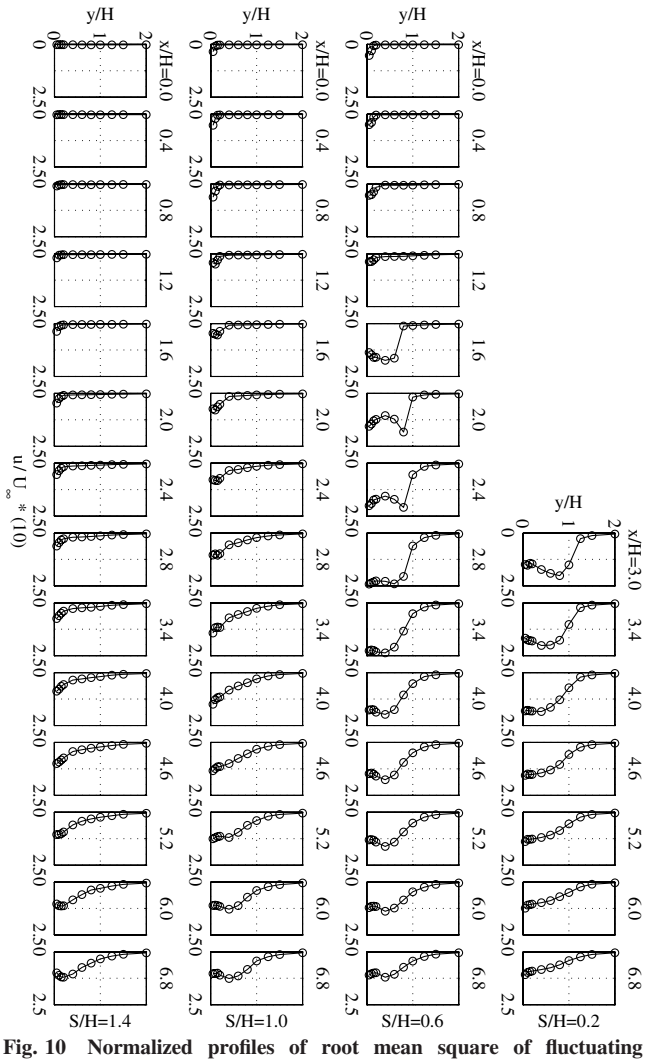

Fig. 10 Normalized profiles of root mean square of fluctuating velocities in the *x* direction.

the bump for the streamwise measurement locations between $x/H = 1.2$ and 2.0. The pressure measurement over the bump showed that for the subcritical Reynolds numbers, the flow over the bump separated before 90 deg over the cylindrical part of the bump (meaning, the part from the ground surface to the half-height of the bump). Because the flow separated before 90 deg at this Reynolds number, it can be concluded using Fig. 7 that the cross-wire probe was very close to, or in the separation region of, some vertical measurement positions for the streamwise measurement locations $x/H = 1.6$, 2.0, 2.4, and 2.8. The horseshoe vortex around the bump prevents the flow over the bump from separating at $y/H = 0.05$ and 0.10. Therefore, the cross-wire data taken between $y/H = 0.10$ and 0.60 from $x/H = 1.6$ to 2.8 are not reliable and should therefore be used with caution, due to the limitation of the hot-wire probe in the separated region on the sides of the bump. On the other hand, the results for these points inside the separation are still useful for seeing where the separation occurred and the size of the separated region.

The bump's upstream effects are detectable at the first measurement location at $x/H = 0.0$ for this spanwise plane. These effects can be grouped as follows: 1) the retardation due to the adverse pressure gradient that appears from the ground surface to the bump's height, 2) the acceleration and push up due to the finite length of the bump, especially after the midheight of the bump, and 3) the negative V component very close to the wall because of the horseshoe vortex. The retardation can be seen in the normalized profiles of streamwise mean velocity in the x direction U at $x/H = 0.0$ and 0.4 (see Fig. 8). The locations downstream of $x/H = 0.8$ in the same plane indicate a slight increase of the U component, which becomes more pronounced at the next profile at $x/H = 1.2$. The reason is mainly due to the acceleration around the bump, as can be seen in the pressure distribution over the ground surface in Fig. 6. The V profile very close to the bump at $x/H = 1.2$ explicitly shows the effect of both the horseshoe vortex (which creates a significant downward motion) and the hemispherical ending of finite size bump (which causes a push up in the positive y direction).

After the reattachment, the U distribution in this spanwise plane has the same features as the spanwise plane closest to the symmetry line of the ground surface: $S/H = 0.2$. At this plane, the flow experiences less downwash compared with the first plane. The root mean square of the fluctuating velocities is slightly different from the profiles shown for $S/H = 0.2$. Even though the streamwise fluctuations are at the same level, peaks appear in the profiles around the bump half-height. This can be attributed the interaction between the extension of the horseshoe vortex and the flow expanding and accelerating after the reattachment point, as shown in Fig. 2a. Fluctuations in the y direction v at $S/H = 0.6$ are found to be smaller than those at $S/H = 0.2$, although the spatial variations are quite similar. This is caused by less downwash at this plane and hence less interaction with the flow developing on the ground. On this spanwise plane, the bump creates a potential flow disturbance upstream of the bump so that the root mean square velocity fluctuation and the Reynolds stress profiles do not show any upstream effects of the bump, unlike the mean velocity. After the reattachment point, the Reynolds stress is mainly due to the interaction of the same physical phenomenon creating the fluctuations.

The spanwise planes $S/H = 1.0$ and 1.4 are similar to each other, but have features that are different from the first two spanwise planes. Because the S direction was moving around the circular ground surface, the angle between the X–Y planes and the plane normal to

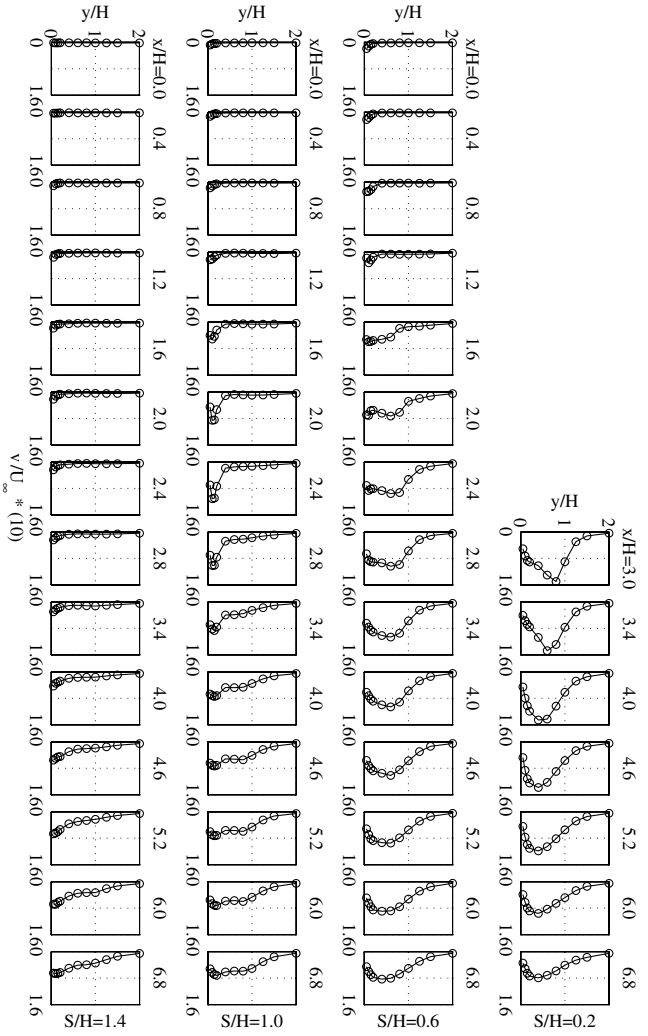

Fig. 11 Normalized profiles of root mean square of fluctuating velocities in the *y* direction.

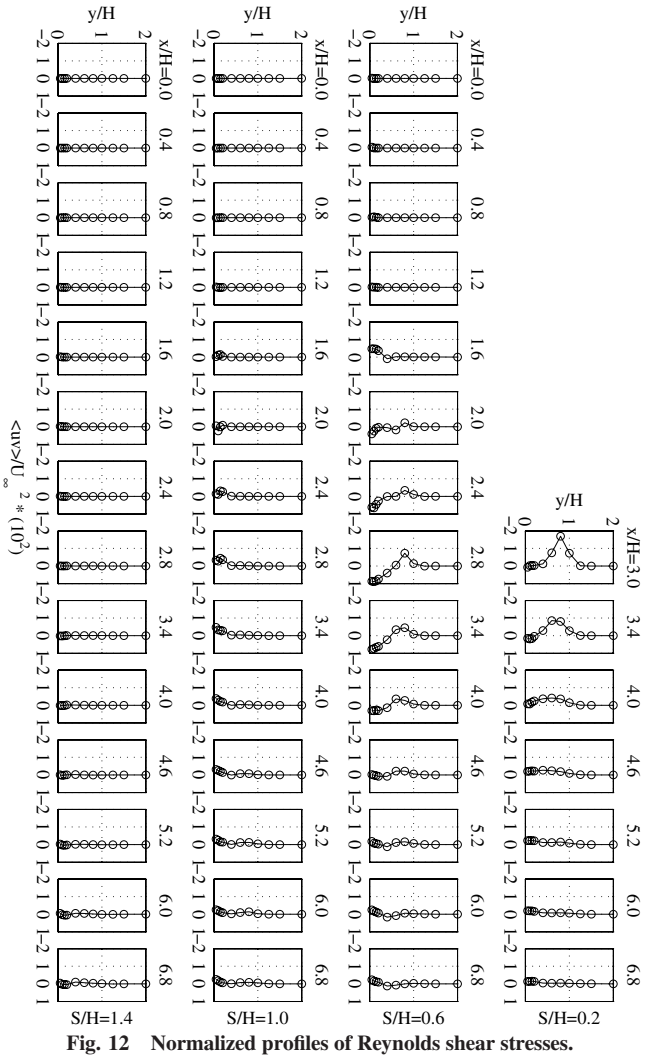

Fig. 12 Normalized profiles of Reynolds shear stresses.

the ground surface increases as S increases. The mean velocity and root mean square of velocity fluctuations in the streamwise direction in Figs. 8 and 10 show that the development of the boundary layer over the ground surface is similar to a planar-boundary-layer development. Contrary to this, profiles of V, v, and $\langle uv \rangle$ do not resemble planar boundary layers. This is because of the measurement planes are not normal to the surface. As S increases, the angle between the X–Y plane and the normal of the cylindrical ground surface increases. Therefore, the results showing the statistical quantities in the y direction differ from those in the wall-normal direction. The x component of the instantaneous velocity (hence, the mean velocity and the root mean square of velocity fluctuations) is not affected, because the response of the cross-wire probe is independent of the orientation around the probe axis parallel to the streamwise direction. As expected, the effect of the bump gradually decreases in the spanwise direction. There is no large disturbance observed on the U component, due to the adverse pressure gradient created by the bump. On the other hand, V profiles indicate an upward motion before and around the bump, because of the free end of the bump. The last plane of measurements is almost free of disturbances created by the bump; hence, profiles of mean velocities, the root mean square of fluctuating velocities, and the Reynolds shear stress resemble an ordinary turbulent boundary layer. The small effects on the mean profiles, such as a positive mean velocity in the y direction around the bump, can be attributed the potential flow disturbances caused by the bump. This does not create any turbulent fluctuations and additional Reynolds shear stresses other than those that exist due to the natural development of the turbulent boundary layer.

IV. Conclusions

Flow visualization, surface-pressure measurements, and instantaneous turbulent velocity measurements were performed for this study. Liquid-crystal paint was found to be useful for visualizing the surface-friction-line pattern on the circular ground surface. The time-averaged thickness of the horseshoe vortex for the Reynolds number 200,000 was about 30% of the bump height. Flow visualization also showed the general flow features over the circular surface, such as the path of the primary separation line of the horseshoe-vortex system and the width of the wake behind the bump and its development. The time-averaged reattachment point was also determined using the visualization results and estimated to occur approximately 110 mm downstream of the bump along the centerline, corresponding to $x/H = 1.1$.

Pressure taps over the bump and ground surface were used to measure the surface pressure. These measurements provided information about the flow topology. On the cylindrical part of the bump, from the half-height of the bump to the ground surface, the flow shows the same characteristics as the finite cylinders in crossflow, in that the flow separates upstream of 90 deg for subcritical Reynolds numbers 33,000 and 67,000. On the other hand, the flow separates downstream of 120 deg for the supercritical Reynolds numbers considered in this study: 133,000 and 200,000. The hemispherical ending of the bump had significant effects on the flowfield, and so the separation over the hemispherical part occurred later. The attached flow after the top of the bump creates a downwash toward the ground surface. The base pressure coefficient was approximately constant at all of the measurement locations at 180 deg, except that at the top of the bump, which does not

experience any separation. However, there were overall small differences in the base pressure coefficients, due to differences in Reynolds numbers.

The size of the recirculating region behind the bump is found to be Reynolds-number-dependent in connection with the separation line on the bump and the strength of the downwash. The flow upstream of the bump is highly affected by its presence, and this effect is also Reynolds-number-dependent. The pressure distribution upstream of the bump is affected by the adverse pressure gradient created by the bump and the horseshoe-vortex system, such that the C_p values of the high Reynolds number flow were larger than that of the low Reynolds number flow.

Statistical information on the mean velocity, the root mean square of velocity fluctuations, and the Reynolds shear stress were obtained using a cross-hot-wire probe. These measurements showed that interaction of the downwash coming from the top of the bump and the turbulent boundary layer developing over the surface creates large turbulence fluctuations. The measured upstream disturbances are the retardation due to the adverse pressure gradient and the push up the flow because of the finite size of the bump. Because the bump creates a potential flow disturbance further upstream, there are no significant changes in the root mean square velocity fluctuation and the Reynolds stress profiles due to the bump. The mean velocity distribution and the distribution of the root mean square of velocity fluctuation in the streamwise direction at the last two measurement planes show that the profiles are similar to planar boundary-layer profiles. The profiles of mean velocities, the root mean square of the velocity fluctuations, and the Reynolds stresses deviates from the ordinary boundary-layer profiles, because these profiles get affected by the angle between the measurement plane and the plane normal to the circular ground surface.

Acknowledgments

The financial support from the Royal Norwegian Air Force (200314650-ENOR) is greatly acknowledged. The authors would like to thank William K. George for his support, reviews, and comments.

References

[1] Chen, S.-S., *Flow-Induced Vibration of Circular Cylindrical Structure*, Springer–Verlag, Berlin, 1987.

[2] Szepessy, S., and Bearman, P., "Aspect Ratio and End Plate Effects on Vortex Shedding from a Circular Cylinder," *Journal of Fluid Mechanics*, Vol. 234, Jan. 1992, pp. 191–217.

[3] Sakamoto, H., and Arie, M., "Vortex Shedding from a Rectangular Prism and a Circular Cylinder Placed Vertically in a Turbulent Boundary Layer," *Journal of Fluid Mechanics*, Vol. 126, Jan. 1989, pp. 147–165.

[4] Farivar, D., "Turbulent Uniform Flow Around Cylinders of Finite Length," *AIAA Journal*, Vol. 19, No. 3, 1981, pp. 275–281.

[5] Ayoub, A., and Karamcheti, K., "An Experiment on the Flow Pas a Finite Circular Cylinder at High Subcritical and Supercritical Reynolds Numbers," *Journal of Fluid Mechanics*, Vol. 118, May 1982, pp. 1–26.

[6] Okamoto, T., and Yagita, M., "The Experimental Investigation on the Flow Past a Circular Cylinder of Finite Length Placed Normal to the Plane Surface in a Uniform Stream," *Bulletin of the JSME*, Vol. 16, No. 95, May 1973, pp. 805–814.

[7] Etzold, F., and Fiedler, H., "The Near-Wake Structure of a Cantilevered Cylinder in a Cross-Flow," *Zeitschrift fur Flugwissenschaften*, Vol. 24, No. 2, 1976, pp. 77–82.

[8] Kawamura, T., Hiwada, M., Hibino, T., Mabuchi, I., and Kumada, M., "Flow around a Finite Circular Cylinder on a Flat Plate: Cylinder Height Greater than Turbulent Boundary Layer Thickness," *Bulletin of the JSME*, Vol. 27, No. 232, 1984, pp. 2142–2151.

[9] Sumner, D., Heseltine, J. L., and Dansereau, O. J. P., "Wake Structure of a Finite Circular Cylinder of Small Aspect Ratio," *Experiments in Fluids*, Vol. 37, No. 5, 2004, pp. 720–730.

[10] Pattenden, R. J., Turnock, S. R., and Zhang, X., "Measurements of the Flow over a Low-Aspect-Ratio Cylinder Mounted on a Ground Plane," *Experiments in Fluids*, Vol. 39, No. 1, 2005, pp. 10–21.

[11] Leder, A., "3D-Flow Structures Behind Truncated Circular Cylinders," 4th ASME/JSME Joint Fluids Engineering Conference, Honolulu, HI, American Society of Mechanical Engineers Paper FEDSM2003-45083, 2003.

[12] Park, C. W., and Lee, S. J., "Effects of Free-End Corner Shape on Flow Structure Around a Finite Cylinder," *Journal of Fluids and Structures*, Vol. 19, No. 2, 2004, pp. 141–158.

[13] Fröhlich, J., and Rodi, W., "LES of the Flow Around a Circular Cylinder of Finite Height," *International Journal of Heat and Fluid Flow*, Vol. 25, No. 3, 2004, pp. 537–548.

[14] Pattenden, R. J., Bressloff, N. W., Turnock, S. R., and Zhang, X., "Unsteady Simulations of the Flow Around a Short Surface-Mounted Cylinder," *International Journal for Numerical Methods in Fluids*, Vol. 53, No. 6, 2007, pp. 895–914.

[15] Devenport, W. J., and Simpson, R. L., "Time-Dependent and Time-Averaged Turbulence Structure Near the Nose of a Wing-Body Junction," *Journal of Fluid Mechanics*, Vol. 210, Nos. 23–55, Jan. 1990, pp. 23–55.

[16] Reif, B. A. P., and Wasberg, C. E., "Numerical Simulations of Flow-Induced Vibrations on Orion P-3C," Norwegian Defence Research Establishment, Rept. 2003/01331, 2003.

[17] Reda, D. C., Wilder, M. C., Farina, D. J., and Zilliac, G., "New Methodology for the Measurement of Surface Shear Stress Vector Distributions," *AIAA Journal*, Vol. 35, No. 4, Apr. 1997, p. 608.

[18] Johansson, P. B. V., and George, W. K., "The Far Downstream Evolution of the High Reynolds Number Axisymmetric Wake Behind a Disk, Part 1: Single Point Statistics," *Journal of Fluid Mechanics*, Vol. 555, May 2006, pp. 363–385.

[19] Tutu, N. K., and Chevray, R., "Cross-Wire Anemometry in High Intensity Turbulence," *Journal of Fluid Mechanics*, Vol. 71, No. 4, 1975, pp. 785–800.

[20] Champagne, F. H., Sleicher, C. A., and Wehrmann, O. H., "Turbulence Measurements with Inclined Hot-Wires, Part 1: Heat Transfer Experiments with Inclined Hot-Wire," *Journal of Fluid Mechanics*, Vol. 28, No. 1, 1967, pp. 153–175.

[21] George, W. K., Beuther, P. D., and Shabbir, A., "Polynomial Calibrations for Hot Wires in Thermally Varying Flows," *Experimental Thermal and Fluid Science*, Vol. 2, No. 2, 1989, pp. 230–235.

[22] Glauser, M. N., "Coherent Structures in the Axisymmetric Turbulent Jet Mixing Layer," Ph.D. Dissertation, State Univ. of New York at Buffalo, Buffalo, NY, 1987.

[23] Naughton, J. W., and Sheplak, M., "Modern Developments in Shear-Stress Measurements," *Progress in Aerospace Sciences*, Vol. 38, Nos. 6–7, 2002, pp. 515–570.

[24] Achenbach, E., "Distribution of Local Pressure and Skin Friction Around a Circular Cylinder in Cross-Flow up to $Re = 5 \times 10^6$," *Journal of Fluid Mechanics*, Vol. 34, No. 4, 1968, pp. 625–639.

[25] Roshko, A., "Experiments on the Flow Past a Circular Cylinder at Very High Reynolds Number," *Journal of Fluid Mechanics*, Vol. 10, No. 3, 1961, pp. 345–356.

[26] Uematsu, Y., and Yamada, M., "Aerodynamic Forces on Circular Cylinders of Finite Height," *Journal of Wind Engineering and Industrial Aerodynamics*, Vol. 51, No. 2, 1994, pp. 249–265.

J. Gore
Associate Editor